

Structure and scaling of inclined temporal gravity currents

Lianzheng Cui , Graham O. Hughes and Maarten van Reeuwijk to

(Received 5 April 2025; revised 23 August 2025; accepted 29 September 2025)

We explore the fundamental flow structure of temporally evolving inclined gravity currents with direct numerical simulations. A velocity maximum naturally divides the current into inner and outer shear layers, which are weakly coupled by momentum and buoyancy exchanges on time scales that are much longer than the typical time scale characterising either layer. The outer layer evolves to a self-similar state and can be described by theory developed for a current on a free-slip slope (Van Reeuwijk et al. 2019, J. Fluid Mech., vol. 873, pp. 786–815) when expressed in terms of outer-layer properties. The inner layer evolves to a quasi-steady state and is essentially unstratified for shallow slopes, with flow statistics that are virtually indistinguishable from fully developed open channel flow. We present the classic buoyancy-drag force balance proposed by Ellison & Turner (1959, J. Fluid Mech., vol. 6, pp. 423–448) for each layer, and find that buoyancy forces in the outer layer balance entrainment drag, while buoyancy forces in the inner layer balance wall friction drag. Using scaling laws within each layer and a matching condition at the velocity maximum, the entire flow system can be solved as a function of the slope angle, in good agreement with the simulation data. We further derive an entrainment law from the solution, which exhibits relatively high accuracy across a wide range of Richardson numbers, and provides new insights into the long runout of oceanographic gravity currents on mild slopes.

Key words: gravity currents, stratified flows, turbulent mixing

1. Introduction

Inclined gravity currents are a type of wall-bounded buoyancy-driven shear flow (Simpson 1999), serving as a critical yet poorly understood mechanism for the transport of various substances in geophysical and engineering environments. Ellison & Turner (1959) were the first to study the dynamics of inclined gravity currents, using laboratory experiments

¹Department of Civil and Environmental Engineering, Imperial College London, London SW7 2AZ, UK **Corresponding author:** Lianzheng Cui, lianzheng.cui22@imperial.ac.uk

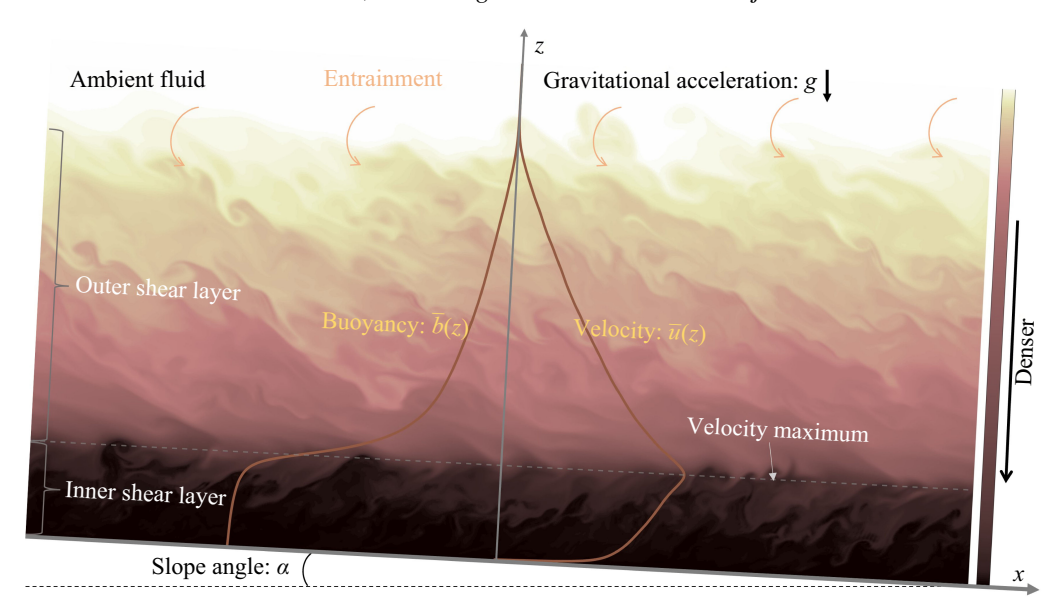


Figure 1. Structure and instantaneous buoyancy field b of an inclined gravity current.

in a sloping laboratory channel to show that the along-slope component of buoyancy in a current is resisted by drag owing to a combination of wall friction and entrainment of ambient fluid. This dynamic equilibrium determines the bulk flow speed in the current.

Establishing a detailed understanding of the dynamics governing an inclined gravity current has proven challenging. In particular, the internal structure of a current generally consists of a relatively dense inner shear layer above the bottom boundary (typically approximated by a boundary layer; Kneller, Bennett & McCaffrey 1999), and an outer shear layer into which overlying ambient fluid is entrained at sufficiently large Reynolds number (Turner 1986). Figure 1 shows an example (from this study) of the instantaneous buoyancy field and internal structure in the body of an inclined gravity current. The two layers are naturally delineated by the level where the along-slope velocity reaches a maximum, the (continuous) mean shear necessarily becomes zero, and the shear production of turbulent kinetic energy (TKE) must vanish (Ellison & Turner 1959). It is apparent, however, that different flow dynamics must govern the outer (free-shear-like) layer and the inner (boundary-layer-like) layer, resulting in differing growth rates and characteristic length scales. Moreover, the flows in each layer are coupled across the level of the velocity maximum.

The modelling of inclined gravity currents in a weakly stratified environment has been relatively well developed. These currents are characterised by a velocity maximum in close proximity to the wall, similar to a turbulent wall jet (Wei, Wang & Yang 2021). Given the minimal role of the inner layer in these scenarios (Sequeiros *et al.* 2010; Luchi *et al.* 2018), a scaling law based on the integral top-hat variables (Ellison & Turner 1959) of the overall current has been widely employed, analogous to the 'outer scaling law' for a wall jet (Wygnanski, Katz & Horev 1992). The flow variables normalised by the integral scales show considerable self-similarity at relatively large slope angles (Krug *et al.* 2013, 2015, 2017; van Reeuwijk *et al.* 2018, 2019; Dieu 2020).

It is unclear if the integral top-hat formulation and disregard of the inner layer remains a valid approach for relatively strongly stratified currents on shallow-angled slopes. At decreasing angles, we expect an increasing portion of the current depth to be occupied by

the inner layer as the driving component of the buoyancy forcing reduces. Indeed, there is accumulating evidence suggesting that the inner and outer layers become decoupled at small angles, driven by a range of underlying mechanisms. Examples include references to a 'zone of strongly limited vertical turbulence' (Luchi et al. 2018), 'anti-diffusive mixing' (Dorrell et al. 2019) and an 'intermediate destruction layer' (Salinas et al. 2021b), all of which contribute to the formation of a transport barrier between the two layers.

In the present study, we conduct direct numerical simulations (DNS) of temporally evolving inclined gravity currents with no-slip bottom boundary conditions for a range of slope inclinations and initial Richardson numbers. Our aim is to investigate the internal structure and coupled dynamics that govern the long-term behaviour of the currents in dynamical equilibrium. The outer layer in our simulations is compared with an inclined temporal gravity current on a free-slip boundary (van Reeuwijk et al. 2019) because the boundary conditions are almost identical in both flows (apart from relaxation of the zero normal buoyancy and momentum flux condition at the base of the outer layer). The inner layer in our simulations is compared with that in a turbulent planar channel flow, including both a closed channel (Lee & Moser 2015) and an open channel (Yao, Chen & Hussain 2022). The ultimate objective of this paper is to develop a complete description of an inclined temporal gravity current by matching the inner- and outer-layer solutions across the velocity maximum.

The simulation set-up and the governing equations are outlined in § 2. In § 3, we examine the evolution of the currents. A scaling model for the outer layer is presented in § 4. We then investigate the interactions between the outer and inner layers in § 5, and develop a scaling model for the inner layer in § 6. The inner-outer scaling models are matched in § 7 to describe the entire current and to model entrainment. Finally, we draw conclusions in § 8.

2. Case description

2.1. Simulation set-up

We consider a negatively buoyant gravity current flowing down a slope of constant angle α after the passage of any transient 'head', such that the current exhibits slow vertical growth induced by entrainment at its upper interface, as shown in figure 1. Periodic boundary conditions are imposed for all flow variables on the lateral boundaries of a finite-sized computational domain. Consequently, the simulations are statistically homogeneous in the streamwise (x) and spanwise (y) directions, but evolve with time. The simulation setup follows the framework established by van Reeuwijk et al. (2019), with the exception of the bottom boundary condition, which in this study is specified as no-slip rather than free-slip. This set-up leads to the evolution of a temporal gravity current, resulting in significant computational savings compared to simulations of a spatially evolving gravity current, especially for shallow-angle cases involving a long evolution process. A detailed description of temporal gravity currents is provided in van Reeuwijk et al. (2019).

If the flow is assumed to be Boussinesq, then the governing equations in the coordinate system in figure 1 may be written as

$$\frac{\partial \mathbf{u}}{\partial t} + \mathbf{u} \cdot \nabla \mathbf{u} = -\rho_a^{-1} \nabla p + v \nabla^2 \mathbf{u} + b\mathbf{e}, \qquad (2.1)$$

$$\frac{\partial b}{\partial t} + \mathbf{u} \cdot \nabla b = \kappa \nabla^2 b, \qquad (2.2)$$

$$\frac{\partial b}{\partial t} + \boldsymbol{u} \cdot \nabla b = \kappa \ \nabla^2 b,\tag{2.2}$$

$$\nabla \cdot \boldsymbol{u} = 0, \tag{2.3}$$

where $\mathbf{u} = (u, v, w)$ is the velocity vector, p is the pressure, $b = (\rho_a - \rho)g/\rho_a$ is the buoyancy, and ρ_a is a reference density (taken to be that of the ambient fluid). The vertical unit vector resolved in the coordinate system is $\mathbf{e} = (-\sin \alpha, 0, \cos \alpha)$, and v and κ are the kinematic viscosity and diffusivity, respectively.

We solve numerically the governing equations using an in-house DNS code SPARKLE, which employs a conservative fourth-order-accurate differencing scheme (Verstappen & Veldman 2003) for spatial discretisation, and an adaptive third-order Adams–Bashforth scheme for explicit time advancement. The code is described in detail by Craske & van Reeuwijk (2015) and has been widely used in simulations of gravity currents (Krug *et al.* 2017; van Reeuwijk *et al.* 2019; Dieu 2020). The grid size Δx of the domain varies between cases to ensure $\Delta x/\eta_K < 3/2$. Here, η_K is a characteristic Kolmogorov length scale defined as $(v^3/\varepsilon_T)^{1/4}$, where $\varepsilon_T = h^{-1} \int \varepsilon \, dz$ is a characteristic dissipation rate. Here, h is a length scale defined in (2.10a). The initial conditions (t = 0) can be written as

$$u(x, y, z) = \begin{cases} u_0, & z \leq h_0, \\ 0, & z > h_0, \end{cases} \quad v(x, y, z) = 0, \quad w(x, y, z) = 0, \quad b = \begin{cases} b_0, & z \leq h_0, \\ 0, & z > h_0, \end{cases}$$

$$(2.4)$$

where u_0 and h_0 each maintain the same value across all simulations, and b_0 is varied to keep $B_0 = \int -b_0 h_0 \sin \alpha \, dz$ constant across the cases. The initial profiles are shown in figure 5(a,b) below. Small random perturbations are introduced to the initial velocity field to trigger turbulence. The computational domain size is $20h_0 \times 20h_0 \times 20h_0$ for all cases. In the streamwise direction, the domain spans approximately ten integral length scales L_T on average, ensuring sufficient data for statistical analysis. Here, $L_T = e_T^{3/2}/\varepsilon_T$, with e_T denoting the characteristic TKE as defined in (2.11). A free-slip wall is imposed on the top boundary to maintain compatibility with the temporal framework. The vertical extent of the domain is significantly larger than the current height so that the top boundary condition has negligible influence on the current itself. Further details are provided in table 1.

2.2. Characteristic quantities

Given the statistical homogeneity in the x and y directions, we spatially average the governing equations, and write the Reynolds-averaged momentum and buoyancy equations as

$$\frac{\partial \overline{u}}{\partial t} + \frac{\partial \overline{w'u'}}{\partial z} = v \frac{\partial^2 \overline{u}}{\partial z^2} - \overline{b} \sin \alpha, \tag{2.5}$$

$$\frac{\partial \overline{b}}{\partial t} + \frac{\partial \overline{w'b'}}{\partial z} = \kappa \frac{\partial^2 \overline{b}}{\partial z^2},\tag{2.6}$$

where $\overline{*} = \int \int * dx \, dy / (L_x L_y)$ represents the spatial averaging operator for the quantity *, L_x and L_y are the dimensions of the domain in the x and y directions, respectively, and a prime represents the departure from the corresponding average, i.e. $*' = * - \overline{*}$. Taking the dot product of \boldsymbol{u} with the momentum (2.1), subtracting the mean kinetic energy $(\overline{\boldsymbol{u}} \cdot \overline{\boldsymbol{u}}/2)$ and averaging over x and y directions, we obtain the TKE budget

$$\frac{\partial e}{\partial t} = -\overline{w'u'}\frac{\partial \overline{u}}{\partial z} + \overline{w'b'}\cos\alpha - \overline{u'b'}\sin\alpha - \varepsilon,$$
(2.7)

where $e = \overline{u_i'^2}/2$ is the TKE, $-\overline{w'u'}(\partial \overline{u}/\partial z)$ is the shear production of TKE, and $\varepsilon = v (\overline{\partial u_i'/\partial x_j})^2$ is the dissipation rate of TKE. Note that the TKE transport terms are neglected.

Simulation	α	Ri_0	Ri_{∞}	Re_{τ}	Resolution $(x \times y \times z)$	t_{ave}/t^*
1N	1°	1.11	0.36	740	1536 ³	20
2N	2°	0.56	0.25	620	1536 ³	13
5N	5°	0.22	0.18	260	$1536^2 \times 1152$	13
10N	10°	0.11	0.14	170	$1536^2 \times 1152$	13
45N	45°	0.02	0.07	100	$1536^2 \times 1024$	7

Table 1. Simulation details: $Ri_0 = -b_0h_0\cos\alpha/u_0^2$ is the initial Richardson number, where b_0 , h_0 , u_0 are the initial buoyancy, layer thickness and velocity, respectively (see (2.4)); Ri_∞ represents the stabilised value of Richardson number Ri when the flow is fully developed, where Ri is defined in (2.10d); the Reynolds number $Re_\tau = u_\tau z_{um}/v$ characterises the inner layer, where $u_\tau = \sqrt{v (\partial \overline{u}/\partial z)|_{z=0}}$ is the friction velocity, and z_{um} is the vertical coordinate of the velocity maximum; t_{ave} is a time interval towards the end of the simulation over which the numerical results are averaged; and $t^* = h_0/\sqrt{B_0}$ is a typical time scale, where $B_0 = \int -b_0h_0 \sin\alpha \, dz$ is the initial buoyancy forcing. The initial Reynolds number $Re_0 = u_0h_0/v$ is 3800, and the Prandtl number $Pr_T = v/\kappa$ is 1.

The integral volume flux Q, momentum flux M and integral buoyancy forcing B of the gravity current are defined here as

$$Q = \int_0^\infty \overline{u} \, dz, \quad M = \int_0^\infty \overline{u}^2 \, dz, \quad B = \int_0^\infty -\overline{b} \sin \alpha \, dz.$$
 (2.8*a*-*c*)

We decompose these quantities into inner and outer components, denoted with subscripts i and o, respectively, i.e.

$$Q = \underbrace{\int_{0}^{z_{um}} \overline{u} \, dz}_{Q_{i}} + \underbrace{\int_{z_{um}}^{\infty} \overline{u} \, dz}_{Q_{o}}, \quad M = \underbrace{\int_{0}^{z_{um}} \overline{u}^{2} \, dz}_{M_{i}} + \underbrace{\int_{z_{um}}^{\infty} \overline{u}^{2} \, dz}_{M_{o}},$$

$$B = \underbrace{\int_{0}^{z_{um}} -\overline{b} \sin \alpha \, dz}_{B_{i}} + \underbrace{\int_{z_{um}}^{\infty} -\overline{b} \sin \alpha \, dz}_{B_{o}},$$

$$(2.9a-c)$$

where z_{um} is the vertical coordinate of the velocity maximum. Note that buoyancy is conserved in the flow, thus B remains constant (equal to B_0). With B_0 prescribed identically across all cases (by adjusting b_0), B is therefore invariant over the full range of slope angles. The characteristic velocity scale u_{T*} , layer thickness h_* , buoyancy b_{T*} and bulk Richardson number Ri_* are defined as

$$h_* = \frac{Q_*^2}{M_*}, \quad u_{T*} = \frac{Q_*}{h_*}, \quad b_{T*} = -\frac{B_*}{h_* \sin \alpha}, \quad Ri_* = \frac{-b_{T*}h_* \cos \alpha}{u_{T*}^2} = \frac{B_*}{u_{T*}^2 \tan \alpha},$$

$$(2.10a-d)$$

respectively, where the subscript * is either omitted, i or o, and is used to characterise the entire current, the inner layer or the outer layer, respectively. In a similar manner, the characteristic scales for TKE e_{T*} are given by

$$\underbrace{\int_{0}^{\infty} e \, \mathrm{d}z}_{e_T h} = \underbrace{\int_{0}^{z_{um}} e \, \mathrm{d}z}_{e_{T_i} h_i} + \underbrace{\int_{z_{um}}^{\infty} e \, \mathrm{d}z}_{e_{T_o} h_o}. \tag{2.11}$$

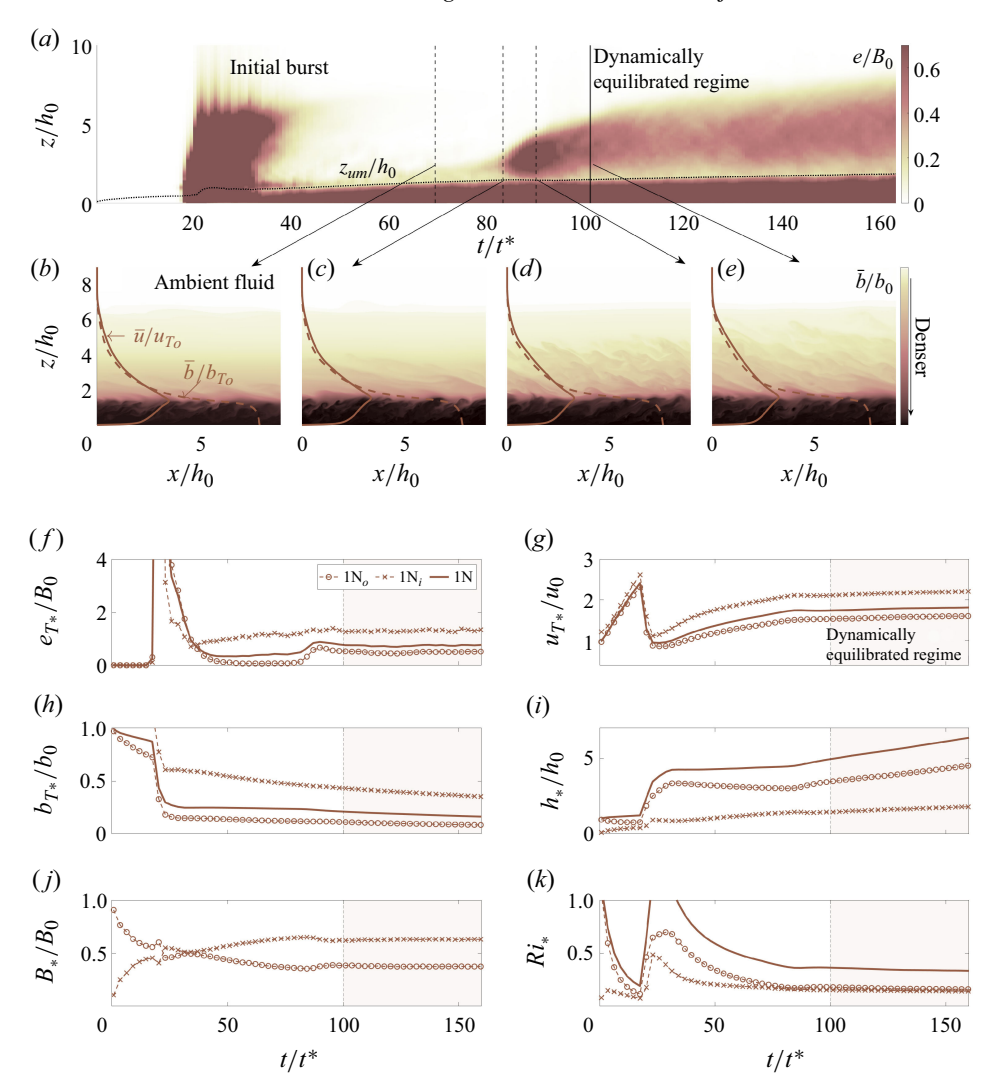


Figure 2. Temporal evolution of (a) dimensionless TKE: e/B_0 for 1N, where the dotted line denotes the boundary between the inner and outer layers, together with the instantaneous buoyancy field \overline{b}/b_0 and profiles of horizontally averaged velocity and buoyancy, \overline{u}/u_{To} and \overline{b}/b_{To} , at (b) $t/t^* = 69.5$, (c) $t/t^* = 83.25$, (d) $t/t^* = 90$ and (e) $t/t^* = 101$. Temporal evolution of normalised (f) e_T , e_{To} , e_{To} , (g) u_T , u_{To} , (h) b_T , b_{To} , b_T ,

3. Temporal evolution

3.1. Inner-outer flow dynamics

As we observe essentially similar evolution processes for all the slope angles considered, we use case 1N as an example to illustrate the dynamics. Figure 2(a) shows the temporal evolution of e(z, t), normalised by B_0 , against t/t^* for case 1N, where $t^* = h/\sqrt{B_0}$ is a typical time scale. Also shown is the location of the velocity maximum z_{um} normalised by h_0 (black dashed line). Instantaneous snapshots at different time intervals of the normalised buoyancy field in figure 2(b-e) show the development of turbulent structures

in the flow. The evolution of layer-specific characteristic flow variables for case 1N are presented in figure 2(f-k); as above, an omitted subscript, i or o is used to denote the overall current, the inner layer or the outer layer, respectively.

An intense initial burst of turbulence associated with shear instabilities is observed for $20 < t/t^* < 40$ in figure 2(a), caused by the sharp initial acceleration (figure 2g) from the initial conditions. This initial burst leads to a noticeable plunge in velocity (see figure 2g), as the mean flow kinetic energy is converted to TKE and potential energy (see the increase of h_* in figure 2i). Consequently, large bulk Richardson numbers arise after the initial burst (see figure 2k) as damping of turbulence and even relaminarisation occurs in the outer layer (see figure 2(a), $50 < t/t^* < 80$). Meanwhile, turbulence is sustained in the inner layer over the whole evolution process.

During the period of damping $(50 < t/t^* < 80)$, the outer layer again accelerates (figure 2g) due to the buoyancy forcing, leading to increased shear and reduced Richardson number (see figure 2k). The outer layer eventually transitions to a turbulent state as the shear instabilities overcome the restoring stratification. The temporal sequence of instantaneous buoyancy fields (figure 2b-e) illustrates the transition to a turbulent regime in the outer layer, which initiates with the onset of instabilities near the velocity maximum, followed by the growth of eddies and vortices. Figure 2(f) quantifies the turbulence level throughout the evolution process, showing the first burst of turbulence and subsequent damping (confined to the outer layer), followed by the eventual transition to a nearly constant turbulence level.

Restricting our attention to the time period $t/t^* > 100$, it is noteworthy that the characteristic velocities u_{Ti} , u_{To} and u_{T} attain nearly constant values (see figure 2g). This behaviour is consistent with the so-called equilibrium state commonly assumed to exist for inclined gravity currents, in which a bulk force balance is achieved (Ellison & Turner 1959; Britter & Linden 1980; Odier, Chen & Ecke 2014; Martin, Negretti & Hopfinger 2019).

The buoyancy variables b_{Ti} , b_{To} and b_{T} shown in figure 2(h) continue to reduce gradually as entrainment of ambient fluid continues to dilute the current and increase the layer thickness (figure 2i). However, the integral buoyancy forcings B_o and B_i (figure 2j) are remarkably invariant, i.e. the total buoyancy in each of the inner and the outer layers is approximately conserved. This behaviour is closely linked to the interaction between the two layers, and is discussed in § 5.1. The bulk Richardson numbers shown in figure 2(k) also attain approximately constant values in the turbulent regime. We will term this state, in which multiple flow parameters take constant characteristic values, the dynamically equilibrated regime, which implies self-similar behaviour in the outer layer and a quasi-steady state in the inner layer; see §§ 4 and 6, respectively.

3.2. Slope angle dependence

Figures 3(a), 3(c) and 3(e) show the evolution of the characteristic thicknesses (h, h_o, h_i) of the currents for different slope angles. The overall thickness h (see figure 3a) and outer-layer thickness h_o (see figure 3c) grow more rapidly on steeper slopes because of relatively vigorous entrainment. Notably, the overall current and the outer layer exhibit a similar normalised growth rate (approximately linear in time in the dynamically equilibrated regime), whilst the inner layer exhibits a much slower growth rate over time.

Figures 3(b), 3(d) and 3(f) plot the bulk Richardson numbers (Ri, Ri_o, Ri_i) as functions of time for different slope angles. In all cases, the various Richardson numbers become essentially constant in the dynamically equilibrated regime and are negatively correlated with slope angle, suggesting a greater role of stratification at a shallower angle.

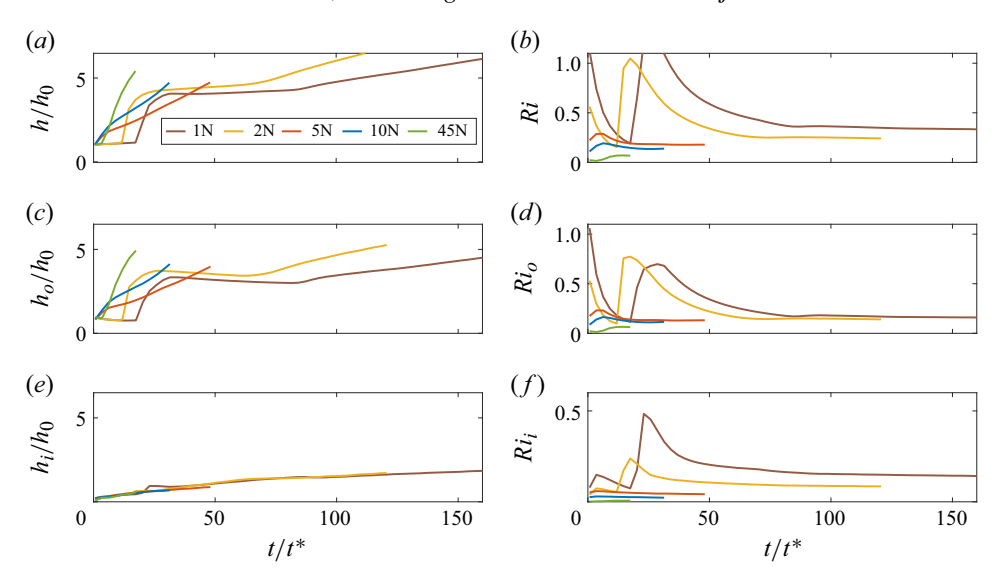


Figure 3. Temporal evolution of overall quantities (a) h/h_0 and (b) Ri, outer-layer quantities (c) h_o/h_0 and (d) Ri_o , and inner-layer quantities (e) h_i/h_0 and (f) Ri_i .

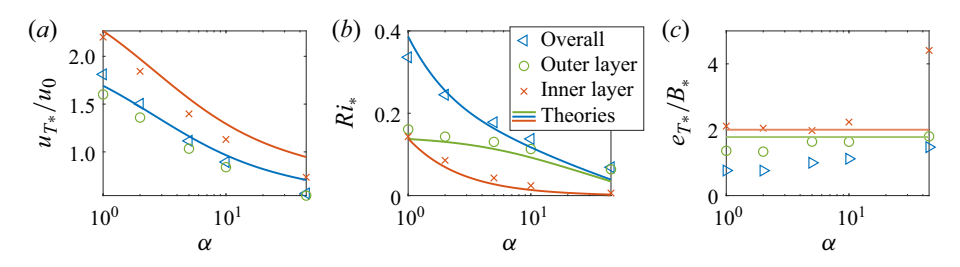


Figure 4. Variation of averaged (a) normalised u_T , (b) Ri, and (c) normalised e_T over t_{ave} in the dynamically equilibrated regime against α in degrees, including the overall, outer and inner quantities for all the slope angles considered. The solid lines in (a) and (b) denote the theoretical predictions from (7.4) and (7.6), respectively. The solid lines in (c) represent the prediction in (4.7) and (6.8).

Figure 4 shows the overall and layer-averaged normalised velocities, Richardson numbers and normalised TKE (the subscript * denoting whether the ordinate in a given panel pertains to an overall or layer-specific quantity) for the currents as a function of slope angle in the dynamically equilibrated regime. The characteristic velocities u_{T*} shown in figure 4(a) attain larger values at shallower angles (u_0 is set to the same value across all the slope angles), reflecting the need for greater shear to overcome stronger stratification and transition the current to the turbulent state. We also observe that $u_T \approx u_{To}$ for all the slope angles.

Figure 4(b) shows that the Richardson numbers in the dynamically equilibrated state increase as the slope angle decreases; Ri_o appears to approach an asymptotic value at a small angle (note the logarithmic scale). This is consistent with the conjecture that stratified shear flows adjust to a 'marginally stable' state (Thorpe & Liu 2009) characterised by a critical Richardson number. Nevertheless, further simulations at milder slopes are needed to confirm the asymptotic behaviour. The overall and inner Richardson numbers Ri and Ri_i , respectively, increase rapidly as the slope angle decreases (see § 6.1 and further discussion in § 7). The normalised TKE is seen in figure 4(c) to be

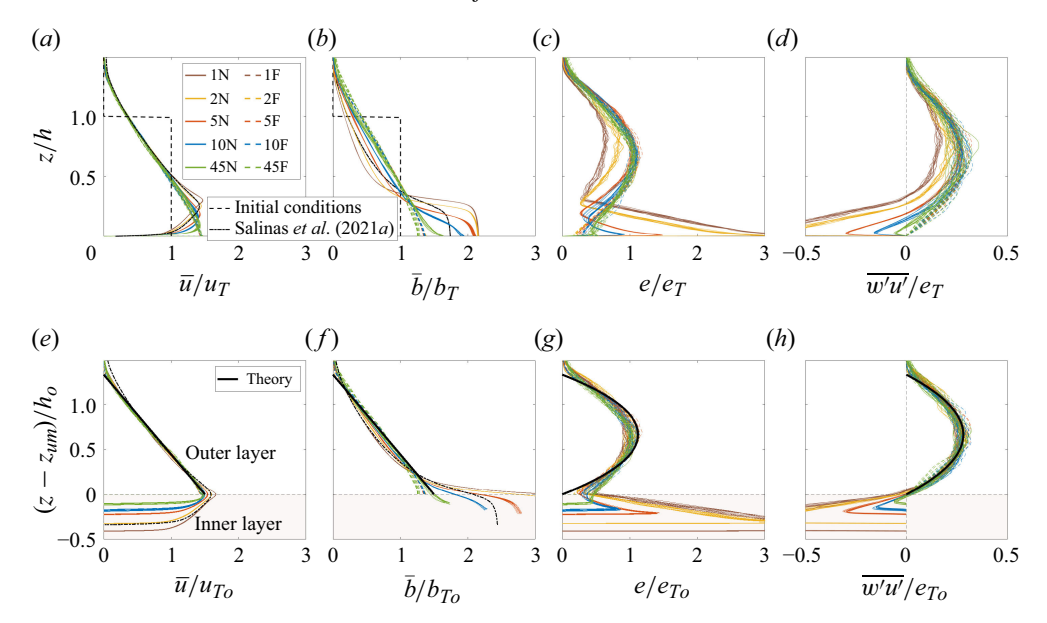


Figure 5. Profiles of $(a) \ \overline{u}/u_T$, $(b) \ \overline{b}/b_T$, $(c) \ e/e_T$ and $(d) \ \overline{w'u'}/e_T$ against scaled height z/h, and $(e) \ \overline{u}/u_{To}$, $(f) \ \overline{b}/b_{To}$, $(g) \ e/e_{To}$ and $(h) \ \overline{w'u'}/e_{To}$ against scaled distance from the velocity maximum $(z-z_{um})/h_o$ (outer-layer scaling). Profiles for each case at a series of times in the dynamically equilibrated regime are plotted. Strong self-similarity and collapse of profiles are observed in the outer layer for all the cases considered when normalisation is based on outer-layer integral quantities. The results for no-slip boundaries (from this study), and free-slip boundaries (adapted from van Reeuwijk *et al.* 2019) are appended with 'N' and 'F', respectively, in the legend (e.g. 5F for a 5° slope with free-slip boundaries). The solid lines in (e-h) represent the predictions from (4.1) and (4.5). The black dashed lines in (a,b) indicate the initial conditions used for all simulations presented in this study. The black dash-dotted lines show results from DNS of a spatially evolving current over slope 2.86°, adapted from Salinas *et al.* (2021a), which almost collapse onto the velocity profiles of case 2N in (a).

approximately constant at the three smallest angles $(1^{\circ}, 2^{\circ}, 5^{\circ})$ in each of the outer and inner layers.

4. Outer-shear-layer scaling

4.1. Self-similar profiles

Figure 5 shows normalised profiles of velocity \overline{u} , buoyancy \overline{b} , TKE e and turbulent shear stress $\overline{w'u'}$ during the dynamically equilibrated regime for all the cases considered, including both no-slip (solid lines) and free-slip (dashed lines) boundary conditions. The results for the free-slip boundary conditions are from van Reeuwijk et al. (2019), and the corresponding dataset is provided in van Reeuwijk (2019). Each profile is scaled by the appropriate integral quantity $(u_T, b_T \text{ or } e_T)$ at the time of sampling in the dynamically equilibrated regime to give figure 5(a-d). Note that $\overline{w'u'}$ is scaled with e_T , and this is discussed in § 4.3. The normalised profiles for the flow variables largely collapse for all free-slip cases, whereas deviations become evident with no-slip boundary conditions.

The observed deviations suggest use of a local scaling based on the integral flow quantities in the outer layer (i.e. u_{To} , b_{To} and e_{To}). Figure 5(e-g) show the profiles of velocity, buoyancy, TKE and Reynolds stress rescaled with the appropriate outer-layer integral quantities. In addition, a normalised vertical ('outer') coordinate $(z - z_{um})/h_o$

is used to facilitate meaningful comparison between the results for free-slip and no-slip boundary conditions (i.e. the vertical coordinate has its origin at the level of the maximum velocity for both types of boundary conditions). Remarkably, all the normalised profiles nearly collapse in the outer layer whether or not an inner layer (corresponding to the region $(z-z_{um})/h_o<0$) is present, indicating analogous self-similar dynamics dominate there. We will therefore refer to the dynamically equilibrated regime in the outer layer as the self-similar regime.

Although there are some deviations from universal forms, these look to be associated primarily with the presence of a strong stratification localised near the velocity maximum for currents on a low-angled no-slip boundary (see § 6.1 for more details). An important observation is that $\overline{w'u'}$ is approximately zero at z_{um} for all cases (see figure 5h), as z_{um} is defined via the velocity maximum, and the gradient diffusion hypothesis (see (4.4)) works reasonably well. This implies that $\partial \overline{u}/\partial z = 0$ and $\overline{w'u'} \approx 0$ hold at the bottom boundary $(z = z_{um})$ of the outer layer in this study and of the currents in van Reeuwijk *et al.* (2019), which underpins the consistency between them as shown in figure 5(e-h).

The DNS results of Salinas *et al.* (2021*a*) for a spatially evolving current over a 2.86° slope show consistent behaviour with the temporally evolving simulations presented in this study in terms of both bulk scaling in figure 5(a,b) and outer-layer scaling in figure 5(c,d). This comparison suggests that temporal currents (at long time) and spatial currents (sufficiently far from the head) share the same self-similar dynamics.

4.2. Approximate self-similar solutions

Given the observed near-collapse of the outer-layer profiles in § 4.1, we now examine the usefulness of the approximate self-similar descriptions developed by van Reeuwijk *et al.* (2019) for inclined currents on a free-slip boundary. We thus propose that the outer-layer profiles are modelled as

$$\overline{u} = \underbrace{a_u B_o^{1/2}}_{u_{To}} \frac{2}{\eta_1^2} (\eta_1 - \eta_o), \quad \overline{b} = \underbrace{-a_b \frac{B_o}{h_o \sin \alpha}}_{b_{To}} \frac{2}{\eta_1^2} (\eta_1 - \eta_o), \quad e = \underbrace{a_e B_o}_{e_{To}} \frac{6\eta_o}{\eta_1^3} (\eta_1 - \eta_o),$$

$$(4.1a-c)$$

where the outer-layer self-similarity variable is defined as $\eta_o = (z - z_{um})/h_o \in [0, \eta_1]$, and the shape factor is $\eta_1 = 4/3$. Note that (4.1a-c) reduce to the form considered by van Reeuwijk *et al.* (2019) for a current on a free-slip boundary upon setting $z_{um} = 0$ and dropping the subscript o.

The coefficients a_u , a_b and a_e depend on the dimensionless parameters of the problem, and need to be determined. We adopt the results of van Reeuwijk *et al.* (2019), who observed that the eddy viscosity, eddy diffusivity, shear production P_S , dissipation rate and turbulent Prandtl number could be parametrised as

$$K_m = c_m \frac{e}{S}, \quad K_\rho = c_\rho \frac{e}{S}, \quad P_s = c_m eS, \quad \varepsilon = c_\varepsilon eS, \quad Pr_T = \frac{c_m}{c_\rho}, \quad (4.2a-e)$$

respectively, where $S = |\partial \overline{u}/\partial z|$ is the absolute strain rate of the mean flow, and $c_m = 0.25 \pm 5.5 \times 10^{-4}$, $c_\rho = 0.31 \pm 2 \times 10^{-3}$ and $c_\varepsilon = 0.21 \pm 2.1 \times 10^{-3}$ are empirical coefficients based on the DNS results. It follows from the success of these scalings in terms of the strain rate S and TKE e that the turbulence is in the shear-dominated regime (Mater & Venayagamoorthy 2014; Krug et al. 2017). Armed with this turbulence closure, van Reeuwijk et al. (2019) integrated the equations for Reynolds-averaged momentum, buoyancy and TKE, (2.5)–(2.7), and used the Von Kármán–Pohlhausen method (Lighthill

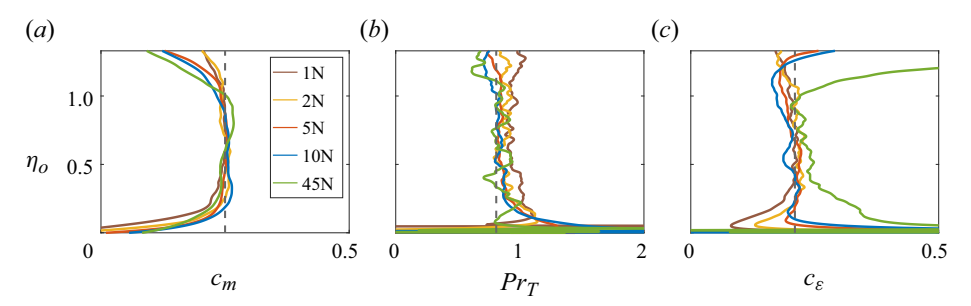


Figure 6. Outer-layer scaling of averaged turbulence parameters over t_{ave} : (a) $c_m = K_m S/e = 0.25 \pm 5.5 \times 10^{-4}$, (b) $Pr_T = c_m/c_\rho = 0.81 \pm 5.2 \times 10^{-3}$ (i.e. $c_\rho \approx 0.31$) and (c) $c_\varepsilon = \varepsilon/(eS) = 0.21 \pm 2.1 \times 10^{-3}$ against scaled distance to velocity maximum $(z - z_{um})/h_o$. The converged values are denoted with the vertical dashed lines.

1950; Spalding 1954; Schlichting & Gersten 2016) to find the coefficients

$$a_{u} = \left(\frac{9}{8} \frac{Pr_{T}(c_{m} - c_{\varepsilon}) \tan \alpha}{\tan \alpha \, Pr_{T} + c_{m}}\right)^{-1/2}, \quad a_{b} = 1.$$
 (4.3*a*,*b*)

Note, however, that the coefficient for the TKE a_e (see (4.1c)) did not follow from the analysis of van Reeuwijk *et al.* (2019), and we evaluate it in the next subsection.

The theoretical solutions given by (4.1)–(4.3) are shown in figure 5(e-h), and are in good agreement with data from the simulations conducted in this study. Notably, the theory predicts that e will tend to zero near $\eta_o = 0$ (i.e. $z = z_{um}$), but because this is not a solid boundary in these simulations, the TKE does not have to be zero there. Despite this, the shear production of TKE is zero at the velocity maximum by definition, and the magnitude of e/e_{To} is indeed close to zero. Therefore, the theory still provides a reasonable approximation.

Figure 6(a-c) show the temporally averaged scaling coefficients defined in (4.2) over times sampled during the self-similar phase. We observe that there is a convincing collapse of profiles across the range of angles, with the converged values matching those from the free-slip cases. We thus conclude that the theory developed by van Reeuwijk *et al.* (2019) can be effectively applied to the outer layer of an inclined current on a no-slip boundary.

In this subsection, we explore if the TKE can be scaled with the integral buoyancy forcing B as suggested by van Reeuwijk *et al.* (2019), thereby allowing all the turbulence quantities in the closure to be related to macroscopic flow quantities. We first assume that the turbulent shear stress $\overline{w'u'}$ can be parametrised in the outer layer (where $\partial \overline{u}/\partial z < 0$) using the gradient diffusion hypothesis and (4.2):

$$\overline{w'u'} = -K_m \frac{\partial \overline{u}}{\partial z} = c_m \frac{e}{S} S = c_m e. \tag{4.4}$$

Substituting for e using (4.1c), we expect $\overline{w'u'}$ to take a self-similar form

$$\overline{w'u'} = c_m e_{T_o} \frac{6\eta_o}{\eta_1^3} (\eta_1 - \eta_o), \qquad (4.5)$$

which is plotted in figure 5(h) and shows good agreement with the DNS data. Note that in contrast with e, we observe that $\overline{w'u'}$ does become zero at $\eta_o = 0$, as discussed in § 4.1. Thus the quadratic profile (4.5) is more appropriate for $\overline{w'u'}$ than for e.

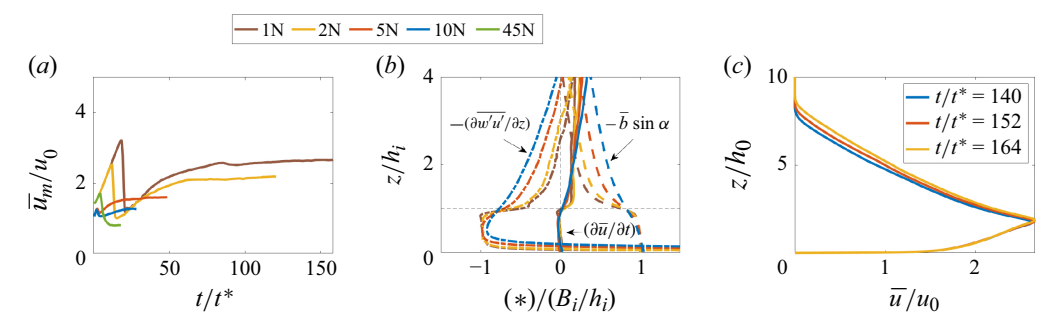


Figure 7. (a) Temporal evolution of the maximum velocity \overline{u}_m . (b) Momentum budgets averaged in the dynamically equilibrated regime over t_{ave} for cases 1N, 2N, 5N and 10N. (c) The instantaneous along-slope velocity profiles in the dynamically equilibrated regime at $t/t^* = 140$, 152, 164 for case 1N. The top legend applies to (a) and (b).

In order to find $a_e (= e_{To}/B_o)$, we first substitute the self-similar expressions (4.1a) and (4.5) into the streamwise momentum (2.5) to give

$$\frac{\partial \overline{u}}{\partial t} = \underbrace{\frac{12c_m e_{To} - 2B_o \eta_1}{h_o \eta_1^3} \eta_o + \frac{2B_o \eta_1 - 6c_m e_{To}}{(h_o) \eta_1^2}}_{-\partial \overline{w'u'}/\partial z - \overline{b} \sin \alpha}.$$

$$(4.6)$$

Secondly, a crucial simplification is motivated by the observation that the characteristic velocity in the outer layer, u_{To} , becomes approximately constant (or only evolves over a relatively large time scale; see figure 2) in the self-similar regime, consistent with the theory described in van Reeuwijk *et al.* (2019). Therefore, the maximum velocity in the outer layer $\overline{u}_m = 3u_{To}/2$ (see (4.1a)) is also expected to become approximately constant in the self-similar regime, consistent with figure 7(a).

Setting $\partial \overline{u}/\partial t \approx 0$ at $\eta_o = 0$ in (4.6) gives $2B_o \eta_1 - 6c_m e_{To} = 0$, thus

$$a_e \equiv \frac{e_{To}}{B_o} = \frac{\eta_1}{3c_m} \approx 1.77$$
 (4.7)

and

$$\frac{\partial \overline{u}}{\partial t} = \frac{9B_o}{8h_o} \eta_o, \quad \eta_o \in [0, \eta_1]. \tag{4.8}$$

The prediction from (4.7) is shown in figure 4(c). Although the shear-dominated scaling mainly applies in the core region ($\eta_o \in [0.5, 1]$) of the outer layer, there is fairly good agreement with the DNS data over the entire outer layer.

Equation (4.8) predicts that the acceleration $\partial \overline{u}/\partial t$ increases with height above the velocity maximum, and is consistent with the instantaneous velocity profiles in figure 7(c). Analysis of the momentum budget shows that the individual terms in (4.6) also vary linearly with height above the velocity maximum in the outer layer (figure 7b). Notably, the gradient of the Reynolds stress and the buoyancy terms are in approximate balance (i.e. no acceleration) at the velocity maximum and in the inner layer. This observation is discussed in detail in § 6.

Over long times, however, $\partial \overline{u}/\partial t$ in the outer layer gradually decreases as h_o increases through entrainment, while B_o remains constant, implying a slow approach towards zero acceleration. In reality, the current is likely disrupted by external effects such as tidal motions or rough topography, which are beyond the scope of the present study.

5. Inner-outer-layer interaction

In this section, we demonstrate that the inner and outer layers are weakly coupled, providing a theoretical foundation for the development of layer-specific scaling laws.

5.1. Integral momentum and buoyancy budgets

The integral momentum and buoyancy equations for the inner and outer layers can be obtained by integrating (2.5) and (2.6) over the respective layer to give

$$\frac{dB_o}{dt} = f_{um} \sin \alpha, \quad \frac{dB_i}{dt} = -f_{um} \sin \alpha,
\frac{dQ_o}{dt} = B_o + m_{um}, \quad \frac{dQ_i}{dt} = B_i - \tau_w - m_{um},$$
(5.1*a-d*)

where $\tau_w = \nu (\partial \overline{u}/\partial z)|_0$ is the shear stress at the lower boundary. The respective exchanges of buoyancy and momentum between the inner and outer layers are

$$f_{um} = -\overline{w'b'}|_{z_{um}} + \overline{b}|_{z_{um}} \frac{\mathrm{d}z_{um}}{\mathrm{d}t} + \kappa \frac{\partial \overline{b}}{\partial z}\Big|_{z_{um}},$$

$$m_{um} = \overline{w'u'}|_{z_{um}} - \overline{u}|_{z_{um}} \frac{\mathrm{d}z_{um}}{\mathrm{d}t}.$$
(5.2a,b)

Here, $\overline{w'b'}|_{z_{um}}$ and $\overline{w'u'}|_{z_{um}}$ are the turbulent buoyancy and momentum fluxes at the level of the velocity maximum z_{um} , respectively, $-\kappa(\partial \overline{b}/\partial z)|_{z_{um}}$ is the molecular buoyancy flux at z_{um} , and $\overline{b}|_{z_{um}}(\mathrm{d}z_{um}/\mathrm{d}t)$ and $\overline{u}|_{z_{um}}(\mathrm{d}z_{um}/\mathrm{d}t)$ are the Leibniz terms (Schatzmann 1978; Davidson 1986; van Reeuwijk *et al.* 2021) representing the effective buoyancy and momentum fluxes associated with a change in the height of the velocity maximum.

Figure 8(a) plots the terms in the integral buoyancy forcing budget of the outer layer ((5.1a) and (5.2a), scaled by B_o/t_o) as a function of slope angle, where $t_o = h_o/u_{To}$ is a typical turnover time scale of the outer layer. The magnitudes of the normalised fluxes are of order 10^{-2} , suggesting that the exchange of buoyancy happens over time scales much longer than t_o . The flux with the largest magnitude is the Leibniz term (especially for small angles), but interestingly, the turbulent and molecular terms counteract it, creating a net buoyancy flux f_{um} that is practically zero for all currents under consideration.

Similarly, figure 8(c) shows the buoyancy flux terms from the inner-layer budget (of equal magnitude and opposite sign to the outer-layer budget), but instead normalised by B_i/t_i , where $t_i = h_i/u_{Ti}$ is a turnover time scale of the inner layer. Here, the scaled budget terms are also of order 10^{-2} , and as in the outer layer, the Leibniz term is in approximate balance with the turbulent and molecular terms. It is apparent that the integral buoyancy forcing B_* can be approximated as constant in each of the inner and outer layers on time scales up to at least t_i and t_o , respectively.

Given that the evolution of the integral buoyancy forcing (dB_*/dt) is not a leading-order term in the inner- and outer-layer budgets at any slope angle considered, the dynamics governing the interface can therefore be regarded as quasi-steady in the self-similar regime, and (5.1a,b) can be approximated as

$$\frac{\mathrm{d}B_o}{\mathrm{d}t} \approx \frac{\mathrm{d}B_i}{\mathrm{d}t} \approx 0,\tag{5.3}$$

which is also consistent with the results in figure 2(j).

Equations (5.1c,d) and (5.2b) present the integral momentum (volume flux) budgets, where B_* acts to accelerate the flow and increase the volume flux. Figure 8(b) illustrates

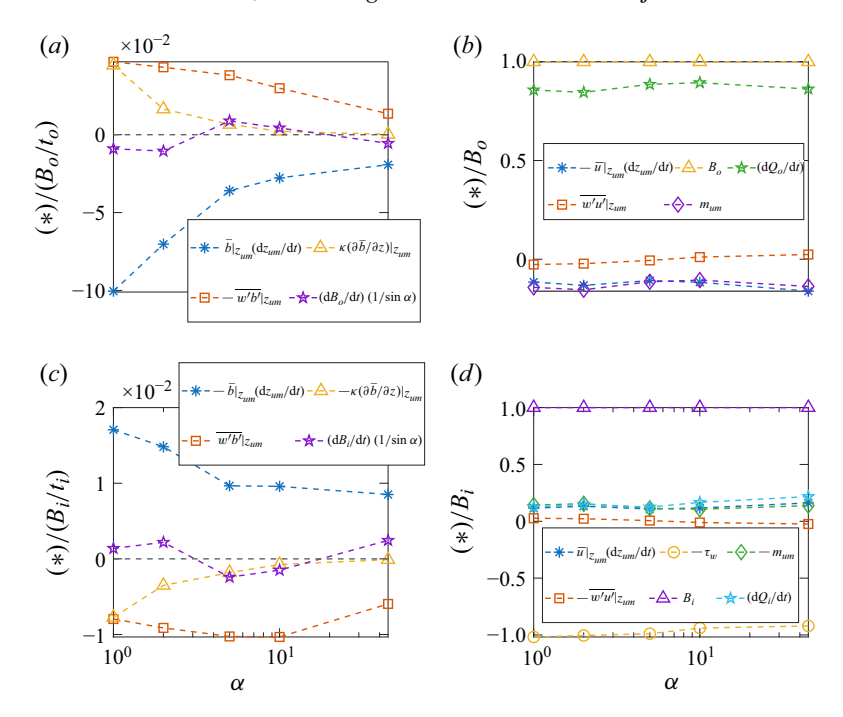


Figure 8. Normalised terms against slope angles for the budgets of (a) outer integral buoyancy forcing, (b) outer volume flux, (c) inner integral buoyancy forcing, and (d) inner volume flux. Note that these term are averaged over t_{ave} in the dynamically equilibrated regime.

the individual terms in the integral momentum budget of the outer layer, normalised by B_o . At all angles, it is clear that the Leibniz term makes the dominant contribution to the momentum exchange between layers m_{um} (see (5.2b)), while the Reynolds stress $\overline{w'u'}|_{z_{um}}$ plays a negligible role. However, this momentum exchange has magnitude approximately $0.15B_o$ at all angles considered, and therefore plays a minor role in modifying the rate of volume flux increase, i.e.

$$\frac{\mathrm{d}Q_o}{\mathrm{d}t} \approx B_o. \tag{5.4}$$

Figure 8(d) shows the integral momentum budget for the inner layer, and we observe a leading-order balance between the buoyancy forcing and bottom shear stress, i.e.

$$B_i \approx \tau_w.$$
 (5.5)

The rate of increase of volume flux in the inner layer is of a similar order to the Leibniz term (towards which the Reynolds stress contribution is negligible, as in the outer layer).

5.2. Layer-specific force balance

Ellison & Turner (1959) showed that gravity currents reach an equilibrium state where the gravitational forces are balanced by 'entrainment drag' and bottom friction. It is useful to interpret this finding in the light of weak interaction between the inner and outer layers.

The starting point is the integral momentum balance for the entire layer, which can be obtained by adding (5.1c) and (5.1d) to give the time derivative of $Q(=u_T h)$:

$$\frac{\mathrm{d}Q}{\mathrm{d}t} = h\frac{\mathrm{d}u_T}{\mathrm{d}t} + u_T\frac{\mathrm{d}h}{\mathrm{d}t} = (B_o + B_i) - \tau_w. \tag{5.6}$$

In terms of top-hat variables (Ellison & Turner 1959), this equation can be written as

$$h\frac{du_T}{dt} = (B_o + B_i) - Eu_T^2 - \tau_w, (5.7)$$

where $E = u_T^{-1} dh/dt$ is the entrainment coefficient of a temporal gravity current (van Reeuwijk *et al.* 2018, 2019). Since u_T is expected to be constant in the dynamically equilibrated regime (Ellison & Turner 1959) (see also figure 2), (5.7) simplifies to

$$B_o + B_i = \tau_w + E u_T^2. (5.8)$$

Given (5.5) and that m_{um} is of a similar magnitude to both $(B_i - \tau_w)$ and $(dQ_o/dt - B_o)$, as observed in figures 8(b) and 8(d), we deduce that

$$B_o \approx E u_T^2$$
. (5.9)

These results support distinct dynamics in the inner and outer layers. Buoyancy in the inner layer primarily overcomes the bottom friction, as shown in figure 7(b), whilst the buoyancy in the outer layer overcomes drag associated with entrainment of ambient fluid. In the absence of significant exchange of momentum, the inner and outer layers are only weakly coupled (subject to the continuity condition at the velocity maximum).

Importantly, our theoretical parametrisation and DNS results show that this weak coupling is not confined to currents on small-angle slopes (with relatively strong stabilising stratification), as conjectured by Salinas *et al.* (2021*b*), but also applies on larger-angle slopes (where the stabilising stratification is relatively weak). This observation signifies that the weak coupling is not a result of a density interface forming near the velocity maximum. Instead, it appears to be a natural behaviour of inclined gravity currents.

Although it has been reported that there is a mismatch between the levels of the velocity maximum and zero turbulent shear stress (Salinas *et al.* 2021*b*; Wei *et al.* 2021), our results indicate that this is not a leading-order effect, and the gradient–diffusion hypothesis remains useful, i.e. both the viscous shear stress and turbulent shear stress change sign and cross zero at the level of the velocity maximum, across which there is essentially no momentum exchange by turbulence or diffusion. This 'decoupling' of the two layers explains why the outer layer behaves independently of bottom friction and much like a current on a free-slip slope described by van Reeuwijk *et al.* (2019).

6. Inner-shear-layer scaling

6.1. Inner-layer profiles

Figure 9(a-d) show the inner-layer profiles of \overline{u} , \overline{b} , e, $\overline{w'u'}$ normalised by the characteristic scales u_{Ti} , b_{Ti} and e_{Ti} , respectively, at a series of times in the dynamically equilibrated regime. We employ z/h_i as the scaled slope-normal coordinate.

We decompose the inner shear layer into two regions: a turbulent wall region (TWR) and a viscous wall region (VWR) defined in terms of the dimensionless wall distance $z^+ = zu_\tau/v$. Figure 9(i) illustrates these regions using case 2N. The VWR is defined up to $z^+ = 10$, rather than $z^+ = 50$ as in traditional boundary layers (Pope 2000), since the viscous contribution to total shear stress becomes negligible beyond $z^+ = 10$ for small-angled gravity currents. The TWR lies above the VWR, with TKE peaking at its lower boundary, and decreasing to a minimum at its upper boundary. The upper boundary of the TWR is defined via a density interface (see figure 9b) in the vicinity of the velocity maximum for small-angled cases. The distinct regions for case 2N are also illustrated in figure 9(a-h) with the same colour scheme as in figure 9(i). Note that the VWR occupies

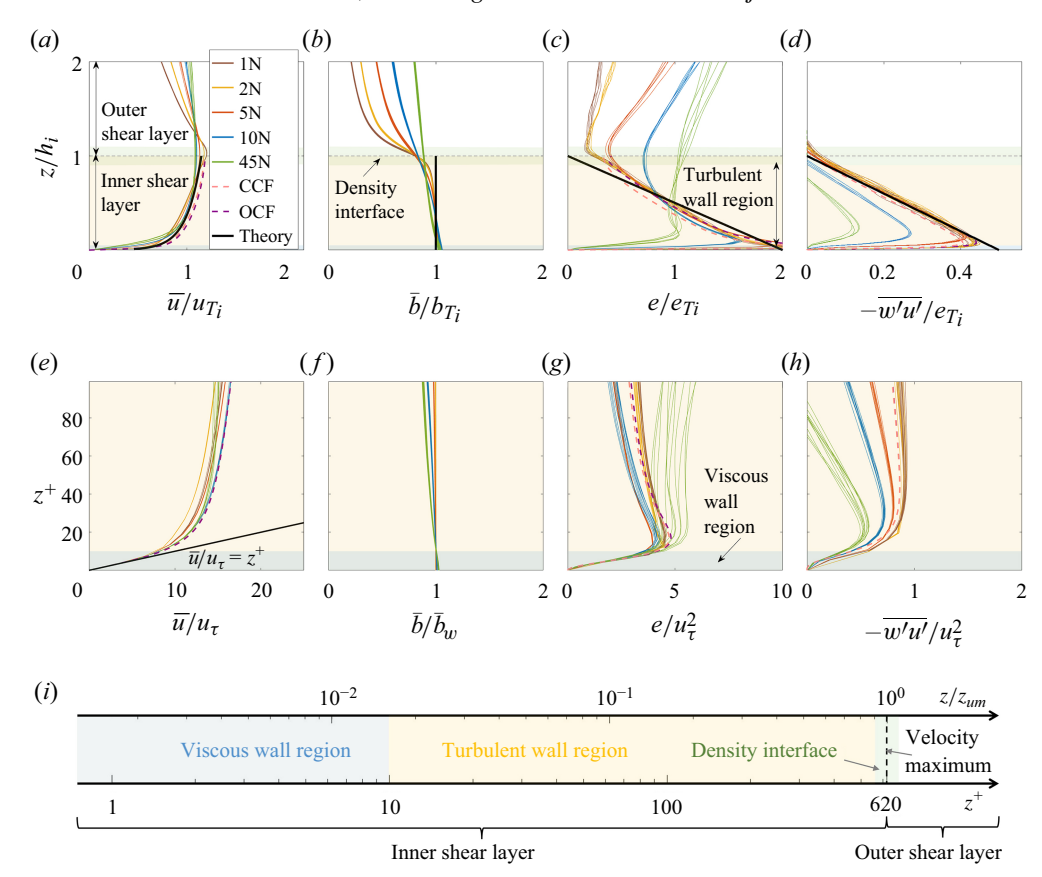


Figure 9. Profiles of spatially averaged (a) \overline{u}/u_{T_i} , (b) \overline{b}/b_{T_i} , (c) e/e_{T_i} and (d) $\overline{w'u'}/e_{T_i}$ against scaled height z/h_i , and (e) \overline{u}/u_{τ} , (f) $\overline{b}/\overline{b}_w$, (g) e/u_{τ}^2 and (h) $\overline{w'u'}/u_{\tau}^2$ against $z^+ = zu_{\tau}/v$. Here, u_{τ} is the friction velocity, and \overline{b}_w is the spatially averaged buoyancy at the wall. Note that the profiles at a series of times in the dynamically equilibrated regime are plotted for each case. Here, CCF indicates the closed channel flow data adapted from Lee & Moser (2015), and OCF indicates the open channel flow data adapted from Yao et al. (2022), both at $Re_{\tau} = 550$. Distinct regions are highlighted with shading, which are depicted in (i) using case 2N with $Re_{\tau} = 620$, including the VWR, the TWR and the density interface, represented by blue, yellow and green, respectively.

only a minor area at the bottom of the inner shear layer in figure 9(a-d), as the vertical coordinate is scaled as z/h_i .

The profiles of scaled mean velocity in figure 9(a) exhibit considerable collapse over a range of times. However, this collapse is not indicative of a self-similar regime like the outer layer; instead, the inner layer reaches a quasi-steady state that evolves over very long time scales. Indeed, figure 7(c) depicts (for slope angle 1°) profiles of mean streamwise velocity \overline{u} scaled by the initial (constant) velocity u_0 in the inner shear layer at different times. The profiles remain nearly unchanged with time because the buoyancy and shear stress gradient are in local balance and $\partial \overline{u}/\partial t \approx 0$ throughout the inner layer, as shown in figure 7(b), i.e.

$$\frac{\partial}{\partial z} \left(\overline{w'u'} - \nu \frac{\partial \overline{u}}{\partial z} \right) \approx -\overline{b} \sin \alpha. \tag{6.1}$$

Furthermore, the profiles of buoyancy in the inner layer (figure 9b) are practically uniform due to strong turbulent mixing, especially for small angles, implying that

$$\overline{w'u'} - \nu \frac{\partial \overline{u}}{\partial z} \approx -\overline{b}z - \tau_w \approx B_i(z/h_i - 1). \tag{6.2}$$

The approximately linear profile of total momentum flux suggested by (6.2) shares a clear analogy with a canonical plane turbulent channel flow subject to constant streamwise pressure gradient, where the momentum balance is given by $\partial (\overline{w'u'} - \nu \partial \overline{u}/\partial z)/\partial z = \partial \overline{p}/\partial x$

In order to explore this connection, profiles corresponding to a closed channel flow (CCF, adapted from Lee & Moser 2015) and an open channel flow (OCF, adapted from Yao et al. 2022) with turbulent Reynolds number $Re_{\tau} = 550$ have been included in figure 9. Note that CCF is subject to no-slip conditions on both the bottom and top boundaries of the channel, with symmetry about the plane at half-height. For the purposes of comparison, the channel half-height is plotted as corresponding to $z/h_i = 1$. In contrast, OCF has a shear-free surface at the top, which is taken to correspond to $z/h_i = 1$. The values of Re_{τ} that characterise the inner shear layer in the gravity currents are a function of slope angle (see table 1 for more details); however, case 2N corresponds to $Re_{\tau} = 620$, similar to that of the selected channel flow comparisons. The scaled velocity profiles of the channel flows shown in figure 9(a) nearly overlap with those for the inner layer in the gravity currents, suggesting the strong similarity of these two flow types. Notably, this similarity is also observed in the spatially evolving DNS results of Salinas et al. (2021a).

Figure 9(c) shows the TKE profiles normalised by e_{Ti} . For small-slope-angle currents, these profiles nearly collapse and decrease approximately linearly with height within the TWR. Deviations become apparent in the TKE profiles between gravity currents on small-and large-angled slopes, the likely explanation for which is that the density interface near the velocity maximum strengthens as the slope angle decreases (figure 9b), acting to suppress turbulence. This explanation is supported by the near collapse of the normalised TKE profiles for the small-angle cases (1N, 2N, 5N) with that for OCF, in which no vertical transport of turbulence is possible at the free surface. The magnitude of normalised TKE for CCF is slightly smaller than for OCF in the TWR, an effect attributed to stronger 'very-large-scale motions' in OCF (Kim & Adrian 1999; Balakumar & Adrian 2007; Yao et al. 2022).

Figure 9(d) shows the normalised turbulent shear stress $\overline{w'u'}/e_{Ti}$, which varies linearly with height throughout most of the inner layer for small-angled gravity currents and all channel flows. This arises because viscous shear stress is negligible compared to turbulent shear stress in the TWR, allowing (6.2) to be simplified as

$$\overline{w'u'} \approx B_i(z/h_i - 1). \tag{6.3}$$

The observed collapse of these profiles upon scaling with e_{Ti} is discussed in § 6.2.

Figure 9(e-h) show the scaled quantities in wall units with a focus on the VWR, which is highlighted using the same colour scheme as in figure 9(i). The velocity profiles in figure 9(e) fully collapse in the VWR ($z^+ < 10$) across all cases, conforming to the well-known relationship $\overline{u}/u_{\tau} = z^+$ in this viscosity-dominated region. Figure 9(f) shows that the buoyancy throughout the VWR is close to the wall buoyancy \overline{b}_w .

The profiles of TKE and $\overline{w'u'}$ normalised by u_{τ}^2 are presented in figures 9(g) and 9(h), respectively, in terms of wall units. The normalised TKE profiles are seen to collapse onto a single curve within the VWR that increases rapidly with height from zero on the lower boundary to a local maximum at the top of the VWR. The normalised $\overline{w'u'}$ profiles for the

2N slope current and the CCF and OCF cases, which all have a similar Re_{τ} , also nearly collapse in the VWR. However, the deviations from this normalised profile for the other slope currents considered suggest a possible Re_{τ} dependence in this scaling.

6.2. Approximate steady-state solution

Upon inspection, we find that an approach analogous to that for the outer layer in §§ 4.2 and 4.3 can also be applied to the inner shear layer. On the basis of the observed collapse in figure 9, approximate solutions are proposed, especially for currents on small-angled slopes:

$$\overline{u} = u_{Ti} f_{ui}(\zeta), \quad \overline{b} = b_{Ti} f_{bi}(\zeta), \quad e = e_{Ti} f_{ei}(\zeta), \quad \zeta = z/h_i \in (0, 1). \tag{6.4}$$

Note that $f_{ui}(\zeta)$, $f_{bi}(\zeta)$ and $f_{ei}(\zeta)$ are expected to be strictly valid only within the TWR. However, as the VWR volume is negligible compared with that of the TWR for the small-angled slope currents, we assume that these functions may be applied throughout the inner shear layer. Taking $f_{bi}(\zeta) \approx 1$ (consistent with figure 9b), we assume that f_{ui} takes a logarithmic form, as for an unstratified boundary layer adjacent to a no-slip surface:

$$f_{u_i}(\zeta) = c_i \ln \zeta + c_{um},\tag{6.5}$$

where c_i is a coefficient to be determined, and $c_{um} = f_{ui}(1) = \overline{u}_m/u_{Ti}$. Consistency with the volume transport decomposition for the inner layer in (2.9a) requires

$$Q_{i} = \int_{0}^{h_{i}} \overline{u} \, dz = u_{T_{i}} h_{i} \int_{0}^{1} f_{u_{i}}(\zeta) \, d\zeta = u_{T_{i}} h_{i} \quad \Rightarrow \quad \int_{0}^{1} f_{u_{i}}(\zeta) \, d\zeta = 1, \quad (6.6)$$

thus $c_i = c_{um} - 1$.

As in § 4.3, we propose that e and $\overline{w'u'}$ in the inner layer (where $\partial \overline{u}/\partial z > 0$ now) are related by the scaling

$$e = K_{mi}S/c_{mi} = -\overline{w'u'}/c_{mi}. \tag{6.7}$$

Note that an additional subscript i is used to distinguish the inner-shear-layer eddy parametrisation coefficient $(c_{mi} \text{ and, later, } c_{\rho i} \text{ and } c_{\epsilon i})$ from that applicable to the outer shear layer. Combining (6.3), (6.4) and (6.7) suggests that f_{ei} takes a linear form (consistent with collapse of the small-angled cases in figure 9c), and consistency with the TKE decomposition for the inner layer (2.11) requires that $\int_0^1 f_{ei}(\zeta) d\zeta = 1$, thus

$$f_{ei} = 2(1 - \zeta), \quad e_{Ti} = e/f_{ei} = B_i/(2c_{mi}).$$
 (6.8)

The approximate solutions proposed in (6.4) and (6.7) can thus be summarised as

$$\frac{\overline{u}}{u_{T_i}} = \underbrace{(c_{um} - 1)\ln \zeta + c_{um}}_{f_{u_i}(\zeta)}, \quad \frac{\overline{b}}{b_{T_i}} = \underbrace{1}_{f_{b_i}(\zeta)}, \quad \frac{e}{e_{T_i}} = -c_{mi} \frac{\overline{w'u'}}{e_{T_i}} = \underbrace{2(1 - \zeta)}_{f_{e_i}(\zeta)}. \quad (6.9a-c)$$

The ratio of u_m to u_{Ti} (i.e. c_{um}) is found from the DNS data to be approximately 1.12. It is interesting to consider the analogy with channel flow using the well-known approximations for the inner layer $\overline{u}/u_{\tau} = c_{\kappa}^{-1} \ln z^+ + C$ and $(\overline{u}_m - u_{Ti})/u_{\tau} = c_{\kappa}^{-1}$ (Pope 2000, equations (7.43) and (7.52) therein), where $c_{\kappa} = 0.41$ is the von Kármán constant, and C is a constant with value approximately 5.2. Comparison with (6.9a) suggests that

$$c_{um} = \frac{c_{\kappa}C + \ln Re_{\tau}}{c_{\kappa}C + \ln Re_{\tau} - 1}, \quad \frac{u_{Ti}}{u_{\tau}} = \frac{1}{(c_{um} - 1)c_{\kappa}},$$
 (6.10)

which is in excellent agreement with the DNS data, e.g. yielding $c_{um} = 1.13$ and $u_{Ti}/u_{\tau} = 18.8$ for $Re_{\tau} = 620$.

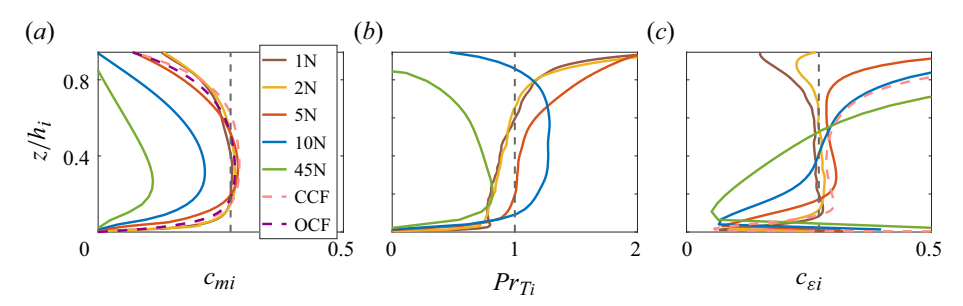


Figure 10. Scaling of inner-layer turbulence parameters averaged over t_{ave} in the dynamically equilibrated regime: (a) $c_{mi} = K_{mi}S/e = 0.27 \pm 0.018$, (b) $Pr_{Ti} = c_{mi}/c_{\rho i} = 1 \pm 0.048$ and (c) $c_{\varepsilon i} = \varepsilon/(eS) = 0.27 \pm 0.012$ against z/h_i . The converged values are denoted with vertical dashed lines.

Figures 10(a), 10(b) and 10(c) show the coefficients c_{mi} , Pr_{Ti} and $c_{\varepsilon i}$ based on the DNS data and the form of the outer-layer scaling in (4.2). We observe that a single value for each scaling coefficient can be applied with reasonable success to the core region of the TWR (where $z/h_i \in [0.25, 0.75]$) in the small-angle slope currents (1N, 2N, 5N) and the channel flows. In particular, c_{mi} converges to approximately 0.27, which is similar to the value of c_m (namely 0.25), indicating comparable sheardriven dynamics in the core regions of the inner and outer layers. Likewise, $c_{\varepsilon i}$ also converges to approximately 0.27, suggesting an approximate balance between turbulence production and dissipation in the quasi-steady state (noting the relation in (4.2c,d)). The converged value of Pr_{Ti} is close to unity, in agreement with the Reynolds analogy. However, Pr_{Ti} exhibits opposite trends in small- and large-angle cases near the velocity maximum, arising from variations in the relative magnitudes of turbulent viscosity and diffusivity. This behaviour presumably suggests the existence of a critical slope angle below which the strong density interface that inhibits mixing spontaneously forms near the velocity maximum. The mechanisms underlying this critical threshold warrant further investigation.

The functions given by (6.9) with $c_{mi} = 0.27$ and $c_{um} = 1.12$ are plotted in figure 9(a–d), and show reasonable agreement with the DNS data for currents on small-angle slopes (e.g. up to 5°) within the TWR. The corresponding prediction from (6.8) that $e_{Ti}/B_i \approx 1.9$ is plotted in figure 4(c) and agrees well with the DNS results for small-angled currents. We suggest that the likely reason for the success of this scaling is that the core region of the TWR is sufficiently far from both the wall and the density interface for the turbulence to be shear-dominated (Mater & Venayagamoorthy 2014), and therefore that parametrising the turbulence using $|\partial \bar{u}/\partial z|$ and e is reasonable.

7. Inner-outer-layer matching condition

7.1. Buoyancy partition

It is clear that the buoyancies in the inner and outer layers $(B_i \text{ and } B_o)$ are the primary forcings in each layer. Therefore, a crucial step in obtaining a closed-form description of a slope current is to predict how buoyancy is partitioned between the layers. Given that $u_T \approx u_{To}$ (figure 2g) and $\tau_w = u_{\tau}^2$, (5.5) and (5.9) can be rewritten as

$$B_o = E u_{To}^2, \quad B_i = u_{\tau}^2.$$
 (7.1*a,b*)

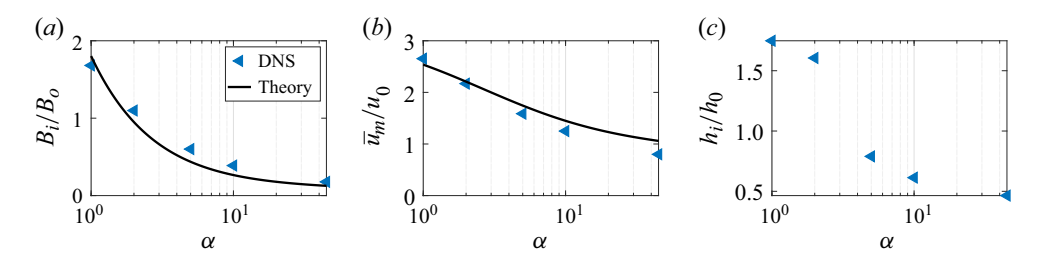


Figure 11. Plots of $(a) B_i/B_o$, $(b) \overline{u}_m/u_0$ and $(c) h_i/h_0$ averaged over t_{ave} in the dynamically equilibrated regime as a function of slope angle α (in degrees). The solid lines in (a,b) denote the theoretical prediction in (7.3), (7.4), respectively.

Combining this with a velocity-matching condition in terms of the self-similar relations $\overline{u}_m = 3u_{To}/2 = c_{um}u_{Ti}$ gives

$$B_o = \frac{4}{9}E\overline{u}_m^2$$
, $B_i = c_{mk}^2\overline{u}_m^2$, and thus $\frac{B_i}{B_o} = \frac{9}{4}c_{mk}^2E^{-1}$, (7.2*a*–*c*)

where $c_{mk} = (c_{um} - 1)c_{\kappa}/c_{um}$. Recalling from (4.1*a*) that $E = B_o/u_{To}^2 = a_u^{-2}$, where a_u is given by (4.3*a*), the predicted dependence of B_i/B_o on α is

$$\frac{B_i}{B_o} = \frac{2c_{mk}^2(Pr_T + c_m/\tan\alpha)}{Pr_T(c_m - c_{\varepsilon})},$$
(7.3)

which is compared in figure 11(a) with B_i/B_o calculated from the DNS data. Reasonably good agreement is found across the range of slope angles α considered, and the ratio B_i/B_o is seen to increase as both the slope angle α and the associated entrainment rate decrease (7.2c). This insight could explain the long runout of submarine gravity currents over mild slopes. As the slope angle reduces: (i) a greater proportion of the buoyancy is confined in the inner layer, where it propagates largely undiluted because of a weak interaction with the outer layer; and (ii) the outer-layer buoyancy also experiences limited dilution due to the reduced entrainment rate.

The maximum velocity \overline{u}_m is determined by substituting (7.3) and $B = B_i + B_o$ into (7.2) to give

$$\overline{u}_{m}(\alpha) = \frac{\sqrt{B_{i}}}{c_{mk}} = \sqrt{\frac{2B(Pr_{T} + c_{m}/\tan\alpha)}{2c_{mk}^{2}(Pr_{T} + c_{m}/\tan\alpha) + Pr_{T}(c_{m} - c_{\varepsilon})}} = \frac{3}{2}u_{To} = c_{um}u_{Ti}. \quad (7.4)$$

The DNS data for \overline{u}_m and u_{T*} shown in figures 11(b) and 4(a) are seen to be well predicted by (7.4). Notably, the characteristic thickness h_i remains a free parameter. Applying buoyancy conservation yields

$$\frac{\int_0^{z_{um}} \overline{b}(t, z) \, dz}{\int_0^\infty \overline{b}(t = 0, z) \, dz} = \frac{b_{Ti} h_i}{b_0 h_0} = \frac{B_i}{B_o + B_i} \quad \Rightarrow \quad \frac{h_i}{h_0} = \frac{B_i / B_o}{1 + B_i / B_o} \frac{b_0}{b_{Ti}}.$$
 (7.5)

Here, B_i/B_o is a function of α as given in (7.3). Equation (7.5) indicates h_i/h_0 (h_0 set to constant) depends on α and the ratio of the initial buoyancy b_0 to the inner characteristic buoyancy b_{Ti} . As shown in figure 11(c), h_i/h_0 attains larger values at smaller angles, with a sharp increase observed between cases 2N and 5N. This sudden rise is likely driven by the dilution due to the initial burst (see $t/t^* \in [20, 40]$ in figure 2), which substantially increases the ratio b_0/b_{Ti} . This observation somewhat suggests that the history of a flow influences its subsequent evolution, as highlighted by Caulfield (2021).

7.2. Entrainment law

Using the self-similar relations for \overline{u}_m , u_{To} and u_{Ti} in § 7.1, we can obtain expressions for Ri_* upon combining (2.10*d*), (7.3), (7.4) and $u_T \approx u_{To}$:

$$Ri_{o} = \frac{9}{8} \frac{Pr_{T} (c_{m} - c_{\varepsilon})}{\tan \alpha Pr_{T} + c_{m}}, \quad Ri_{i} = \frac{c_{mk}^{2} c_{um}^{2}}{\tan \alpha},$$

$$Ri = \frac{9}{8} \frac{2c_{mk}^{2} (Pr_{T} + c_{m}/\tan \alpha) + Pr_{T} (c_{m} - c_{\varepsilon})}{\tan \alpha Pr_{T} + c_{m}}.$$
(7.6*a*-*c*)

The predictions for these Richardson numbers are plotted in figure 4(b), with good agreement apparent for small slope angles. Equation (7.6a) indicates that the outer-layer Richardson number Ri_o increases and approaches a finite limit $(Ri_{om} \approx 9 \ Pr_T \ (c_m - c_{\varepsilon})/8c_m)$ as α decreases $(\tan \alpha \ll c_m/Pr_T)$. This limiting value suggests that the outer layer remains marginally stable and weakly stratified at all the slope angles considered here. However, Ri and Ri_i continue to increase as the slope angle decreases. Notably, Ri_i loses physical relevance for small-angled cases, as the inner layer is nearly well-mixed in these scenarios. Richardson number Ri is directly related to the buoyancy partition, as shown by the following relationship derived from (2.10d) with $u_T \approx u_{To}$:

$$Ri/Ri_o = B/B_o. (7.7)$$

Therefore, the increase in Ri with decreasing α essentially reflects the increasing proportion of the integral buoyancy held in the inner layer.

As we have shown in this study that entrainment is associated with the outer layer dynamics in a slope current, we now adapt the entrainment law derived by van Reeuwijk *et al.* (2019) for currents on free-slip boundaries ((4.24) and (4.25) therein). Using (7.7) to relate Ri and Ri_0 , their theoretical expression can be rewritten as

$$E = \frac{c_m}{Pr_T} (Ri_{om} - Ri_o) = \frac{c_m}{Pr_T} \left(Ri_{om} - Ri \frac{B_o}{B} \right), \quad Ri_{om} = 0.15,$$
 (7.8)

which, with (7.2c), gives the entrainment law as an explicit function of Ri:

$$E = \frac{c_m}{Pr_T} \left(Ri_{om} - \frac{E Ri}{9c_{mk}^2/4 + E} \right) \implies$$

$$E = \frac{\sqrt{(c_m Ri/Pr_T + c_{R1})^2 + c_{R2}} - c_m Ri/Pr_T - c_{R1}}{2}, \quad (7.9)$$

where $c_{R1} = 9c_{mk}^2/4 - c_m Ri_{om}/Pr_T$ and $c_{R2} = 9c_{mk}^2 c_m Ri_{om}/Pr_T$ are constants.

Figure 12 shows the predicted entrainment rate E as a function of densitometric Froude number $Fr = 1/\sqrt{Ri}$. The present theory (7.9) (solid black line) is shown together with entrainment models from van Reeuwijk *et al.* (2019) as a dashed line, Ellison & Turner (1959) as a dash-dotted line, and Parker *et al.* (1987) as a dotted line, along with a broad dataset (denoted by coloured symbols) from laboratory experiments, DNS and field observations, as compiled by Odier *et al.* (2014) and Salinas *et al.* (2019) (details provided in the caption). The present data are in good agreement with the present theory, and both show consistency with the spatially evolving DNS results of Salinas *et al.* (2022), suggesting that similar entrainment processes operate in both temporal and spatial configurations.

The classical parametrisation based on the experimental data from Ellison & Turner (1959) (proposed by Turner 1986) aligns well with the high-Fr data, but shows a different

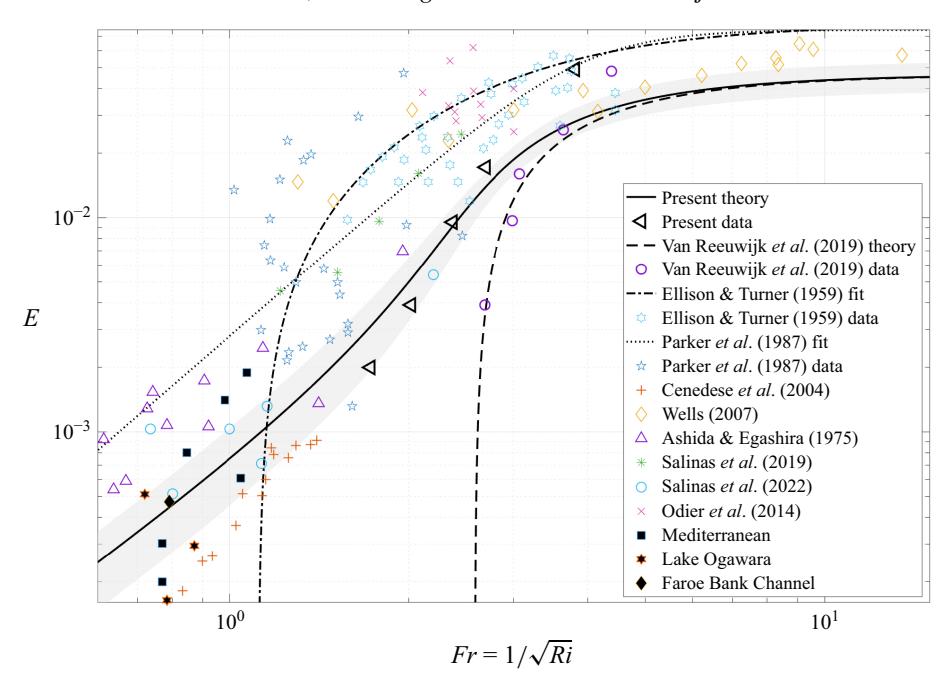


Figure 12. Entrainment rate E against $Fr = 1/\sqrt{Ri}$. The black solid line and triangles denote the prediction in (7.9) and the present DNS data, respectively. The shaded band represents the 95 % uncertainty interval of the present theory obtained via Monte Carlo uncertainty analysis. The data and theory from van Reeuwijk *et al.* (2019), Salinas *et al.* (2022), and the previous data and fitted functions compiled by Odier *et al.* (2014) and Salinas *et al.* (2019) are also shown – incorporating the studies by Ellison & Turner (1959), Ashida & Egashira (1975), Parker *et al.* (1987), Cenedese *et al.* (2004), Wells (2007), Odier *et al.* (2014) and Salinas *et al.* (2019), together with field data (filled markers) collected from the Mediterranean, Lake Ogawara and the Faroe Bank Channel). The dataset for this plot is available at Cui (2025).

asymptotic behaviour at low Fr (with E dropping to 0 at a critical Fr value beyond the range accessible to their experiments). The parametrisation fitted by Parker $et\ al.$ (1987) has asymptotic behaviour that is more consistent with the data and offers better overall performance, but its functional form lacks a solid theoretical basis.

The theoretical model of van Reeuwijk *et al.* (2019) predicts E as a function of the outer-layer Richardson number Ri_o , as described by (7.8). A comparison between their prediction $E(Ri_o)$ and the present theoretical prediction E(Ri) (see (7.9)), presented in figure 12, highlights the significant role that the outer-layer dynamics is likely to play in many slope current applications. As indicated by (7.7), $Ri \approx Ri_o$ at large Fr (corresponding to steep slopes), where the integral buoyancy forcing is primarily confined within the outer layer (i.e. $B_o/B \approx 1$). Under these conditions, the two predictions are in close agreement, while increasing deviations are observed as Fr decreases (note, however, that the entrainment rate remains consistent for the same slope angle). Both theories suggest a maximum entrainment rate $E_m = c_m Ri_{om}/Pr_T \approx 0.046$ as Fr approaches infinity, which is in good agreement with the value 0.04 proposed by Wells, Cenedese & Caulfield (2010).

The present theory indicates that entrainment is not completely suppressed at a critical Ri(Fr), but rather asymptotes towards 0 as $Ri \to \infty$ ($\alpha \to 0$), consistent with the level of TKE in the outer layer e_{To} that scales with B_o (see (4.7)). Notably, this differs conceptually from the hypothesis of 'continued (high-Richardson-number) mixing' associated with intermittent turbulence under strong stratification (see e.g. Wells *et al.* 2010). Despite

Ri approaching infinity as α decreases towards 0, the outer layer herein remains weakly stratified, with Ri_o asymptotically approaching Ri_{om} as shown in figure 4(b). Crucially, the present theory shows good agreement with the field data (filled symbols in figure 12), offering a physical basis and the prospect of general applicability to flows at small Fr of geophysical relevance.

8. Conclusion

In this paper, we explored the fundamental flow structure and scaling laws of temporal inclined gravity currents using direct numerical simulations. The simulations run for a duration that is sufficient to reach a dynamically equilibrated (time-evolving) regime across a range of slope angles. We find that the slope currents comprise a relatively well-mixed inner layer adjacent to the slope that is overlain by a density-stratified outer layer. The inner and outer layers are delineated by the level at which a velocity maximum is situated. In the dynamically equilibrated regime, the outer layer exhibits self-similar dynamics identical to those of gravity currents on free-slip slopes studied by van Reeuwijk et al. (2019). The inner layer resembles fully developed plane turbulent channel flow, in which the shear stress decreases linearly with distance from the wall, and the logarithmic velocity defect law applies.

At small slope angles, a density interface is observed to form in the vicinity of the velocity maximum. Although the presence of a density interface has been interpreted in the literature as a decoupling between the inner and outer layers (Dorrell *et al.* 2019; Salinas *et al.* 2021*b*), our simulations indicate that the two layers are effectively decoupled for all slope angles investigated. As a consequence, the integral buoyancy and volume flux in each layer evolve nearly independently (subject to the continuity condition at the maximum). The classic force balance (Ellison & Turner 1959), in which buoyancy forces are countered by entrainment drag and wall friction, can be further refined: the outer-layer buoyancy forcing is responsible for overcoming the entrainment drag, whilst the inner-layer buoyancy forcing counteracts the wall friction. This force balance, together with the weak coupling between the inner and outer layers (becoming even weaker at smaller slopes), underpins the dynamical equilibrium observed in both the inner and outer layers across all slope angles considered.

Based on the flow structure, we have developed a theoretical description of an inclined gravity current by matching the dynamics of a turbulent wall-bounded inner layer and a self-similar outer layer at the velocity maximum. The theory predicts the flow quantities as functions of slope angle only, and is expected to best characterise currents with higher friction Reynolds numbers Re_{τ} (corresponding to smaller slope angles in this study), for which the inner layer is more analogous to a pressure-driven channel flow, and the core region of the layer is sufficiently far from both the wall and the density interface for the turbulence to be shear-dominated (Mater & Venayagamoorthy 2014).

An important observation in both the simulations and the theory is that the ratio of the integral buoyancies in the inner and outer layers increases as the slope angle decreases. This insight offers a potential explanation for the long runout of submarine gravity currents along mild slopes: as the slope angle reduces, first, a greater proportion of the buoyancy is confined in the inner layer (where it remains largely undiluted because of a weak interaction with the outer layer) and, second, entrainment of ambient fluid into the outer layer (and consequent dilution of its buoyancy) is also reduced. The theory also gives the entrainment rate E as a function of the overall Richardson number Ri. The entrainment model allows application to small slope angles of oceanographic relevance, and aligns well with field data collected from the Mediterranean, Lake Ogawara and the Faroe Bank

Channel. Although the minimum slope angle considered in the simulations here is 1°, the inner-outer scaling offers a solid physical basis from which the theoretical predictions have been extrapolated to the milder slopes that characterise a range of geophysical flows. While the present analysis concerns buoyancy fields created by variations in species concentration, the results, with appropriate caution, also apply to turbidity currents involving very fine particles (i.e. relatively slow settling velocities).

One interesting question posed by this study is whether inclined gravity currents can reach a strongly stratified regime – specifically, whether they can enter the so-called (high Richardson number) 'right flank' (Linden 1979; Wells *et al.* 2010; Caulfield 2021). Our results indicate that even though the bulk Richardson number Ri can exceed 1/4 (and approach infinity when $\alpha \to 0$), a threshold often associated with 'marginal stability' (Thorpe & Liu 2009), neither the inner layer nor the outer layer becomes strongly stratified. In contrast, the outer Richardson number Ri_0 remains below 1/4 regardless of the slope angle, and appears to be a more relevant measure of the dynamical importance of the stratification.

While the extrapolated flow behaviour at high Richardson numbers (i.e. small slope angles) appears consistent with the 'marginal stability' conjecture and with geophysical observations, further simulations at even smaller inclination angles are required to confirm this. In particular, it remains to be seen whether the so-called 'subcritical regime' at shallow slopes (Salinas *et al.* 2021*b*) falls within the scope of the present theoretical framework. Moreover, although the temporal and spatial formulations exhibit a high degree of consistency in terms of self-similarity, inner–outer layer structure and entrainment, further research is needed to fully understand their dynamical linkage (e.g. whether they generate the same coherent structures) and to extend the applicability of the present theory to a broader range of gravity current scenarios. Nevertheless, the results presented in this paper highlight the importance of a layer-wise perspective for analysing complex geophysical wall-bounded stratified flows, where an (inner) unstratified boundary layer can coexist with an (outer) stratified shear layer. An approach based on bulk properties only risks overlooking the key physics and internal processes governing such flows.

Funding. The authors acknowledge the UK Turbulence Consortium (EPSRC grants EP/R029326/1 and EP/X035484/1) for the grand challenge project that provided the computational resources for this work. L.C. acknowledges the Skempton scholarship and financial support from the China Scholarship Council for his PhD study. G.H. acknowledges support from the EPSRC project 'D*stratify' (grant no. EP/V033883/1).

Declaration of interests. The authors report no conflict of interest.

Data availability statement. The data that support the findings of this study are openly available at https://doi.org/10.5281/zenodo.17268071.

REFERENCES

ASHIDA, K. & EGASHIRA, S. 1975 Basic study on turbidity currents. *Proc. Japan Soc. Civ. Engrs* 1975, 37–50.

BALAKUMAR, B.J. & ADRIAN, R.J. 2007 Large- and very-large-scale motions in channel and boundary-layer flows. *Phil. Trans. R. Soc. A: Math. Phys. Engng Sci.* **365** (1852), 665–681.

BRITTER, R.E. & LINDEN, P.F. 1980 The motion of the front of a gravity current travelling down an incline. *J. Fluid Mech.* **99** (3), 531–543.

CAULFIELD, C.P. 2021 Layering, instabilities, and mixing in turbulent stratified flows. *Annu. Rev. Fluid Mech.* 53, 113–145.

CENEDESE, C., WHITEHEAD, J.A., ASCARELLI, T.A. & OHIWA, M. 2004 A dense current flowing down a sloping bottom in a rotating fluid. *J. Phys. Oceanogr.* **34** (1), 188–203.

- CRASKE, J. & VAN REEUWIJK, M. 2015 Energy dispersion in turbulent jets. Part 1. Direct simulation of steady and unsteady jets. J. Fluid Mech. 763, 500–537.
- CUI, L. 2025 Dataset for 'structure and scaling of inclined temporal gravity currents'. Zenodo, [Data Set]. Available at: https://doi.org/10.5281/zenodo.17268071.
- DAVIDSON, G.A. 1986 A discussion of Schatzmann's integral plume model from a control volume viewpoint. J. Appl. Meteorol. Climatol. 25 (6), 858–867.
- DIEU, E.A. 2020 Mixing and transport in inclined gravity currents. *PhD thesis*, Imperial College London, London, UK.
- DORRELL, R.M., PEAKALL, J., DARBY, S.E., PARSONS, D.R., JOHNSON, J., SUMNER, E.J., WYNN, R.B., ÖZSOY, E. & TEZCAN, D. 2019 Self-sharpening induces jet-like structure in seafloor gravity currents. *Nat. Commun.* 10 (1), 1381.
- ELLISON, T.H. & TURNER, J.S. 1959 Turbulent entrainment in stratified flows. J. Fluid Mech. 6 (3), 423-448.
- KIM, K.C. & ADRIAN, R.J. 1999 Very large-scale motion in the outer layer. Phys. Fluids 11 (2), 417-422.
- KNELLER, B.C., BENNETT, S.J. & MCCAFFREY, W.D. 1999 Velocity structure, turbulence and fluid stresses in experimental gravity currents. *J. Geophys. Res.: Oceans* **104** (C3), 5381–5391.
- KRUG, D., HOLZNER, M., LÜTHI, B., WOLF, M., KINZELBACH, W. & TSINOBER, A. 2013 Experimental study of entrainment and interface dynamics in a gravity current. *Exp. Fluids* **54** (5), 1530.
- KRUG, D., HOLZNER, M., LÜTHI, B., WOLF, M., KINZELBACH, W. & TSINOBER, A. 2015 The turbulent/non-turbulent interface in an inclined dense gravity current. *J. Fluid Mech.* **765**, 303–324.
- KRUG, D., HOLZNER, M., MARUSIC, I. & VAN REEUWIJK, M. 2017 Fractal scaling of the turbulence interface in gravity currents. *J. Fluid Mech.* 820, R3.
- LEE, M. & MOSER, R.D. 2015 Direct numerical simulation of turbulent channel flow up to $re_{\tau} = 5200$. J. Fluid Mech. 774, 395–415.
- LIGHTHILL, M.J. 1950 Contributions to the theory of heat transfer through a laminar boundary layer. *Proc. R. Soc. Lond. A: Math. Phys. Sci.* **202** (1070), 359–377.
- LINDEN, P.F. 1979 Mixing in stratified fluids. Geophys. Astrophys. Fluid Dyn. 13 (1), 3-23.
- LUCHI, R., BALACHANDAR, S., SEMINARA, G. & Gary. 2018 Turbidity currents with equilibrium basal driving layers: a mechanism for long runout. *Geophys. Res. Lett.* 45 (3), 1518–1526.
- MARTIN, A., NEGRETTI, M.E. & HOPFINGER, E.J. 2019 Development of gravity currents on slopes under different interfacial instability conditions. J. Fluid Mech. 880, 180–208.
- MATER, B.D. & VENAYAGAMOORTHY, S.K. 2014 A unifying framework for parameterizing stably stratified shear-flow turbulence. *Phys. Fluids* **26** (3), 036601.
- ODIER, P., CHEN, J. & ECKE, R.E. 2014 Entrainment and mixing in a laboratory model of oceanic overflow. *J. Fluid Mech.* **746**, 498–535.
- PARKER, G., GARCIA, M., FUKUSHIMA, Y. & YU, W. 1987 Experiments on turbidity currents over an erodible bed. *J. Hydraul. Res.* 25 (1), 123–147.
- POPE, S.B. 2000 Turbulent Flows. Cambridge University Press.
- VAN REEUWIJK, M., KRUG, D. & HOLZNER, M. 2018 Small-scale entrainment in inclined gravity currents. Environ. Fluid Mech. 18 (1), 225–239.
- VAN REEUWIJK, M., HOLZNER, M. & CAULFIELD, C.P. 2019 Mixing and entrainment are suppressed in inclined gravity currents. *J. Fluid Mech.* 873, 786–815.
- VAN REEUWIJK, M. 2019 Dataset for 'mixing and entrainment are suppressed in inclined gravity currents'. Zenodo, [Data Set]. Available at: https://doi.org/10.5281/zenodo.17259531.
- VAN REEUWIJK, M., VASSILICOS, J.C. & CRASKE, J. 2021 Unified description of turbulent entrainment. J. Fluid Mech. 908, A12.
- SALINAS, J.S., BALACHANDAR, S. & CANTERO, M.I. 2021a Control of turbulent transport in supercritical currents by three families of hairpin vortices. *Phys. Rev. Fluids* 6 (6), 063801.
- SALINAS, J.S., BALACHANDAR, S., SHRINGARPURE, M., FEDELE, J., HOYAL, D., ZUNIGA, S. & CANTERO, M.I. 2021b Anatomy of subcritical submarine flows with a lutocline and an intermediate destruction layer. *Nat. Commun.* 12 (1), 1649.
- SALINAS, J.S., CANTERO, M.I., SHRINGARPURE, M. & BALACHANDAR, S. 2019 Properties of the body of a turbidity current at near-normal conditions: 1. Effect of bed slope. *J. Geophys. Res.: Oceans* **124** (11), 7989–8016.
- SALINAS, J.S., ZÚÑIGA, S., CANTERO, M.I., SHRINGARPURE, M., FEDELE, J., HOYAL, D. & BALACHANDAR, S. 2022 Slope dependence of self-similar structure and entrainment in gravity currents. J. Fluid Mech. 934, R4.
- SCHATZMANN, M. 1978 The integral equations for round buoyant jets in stratified flows. Z. Angew. Math. Phys. 29 (4), 608–630.
- SCHLICHTING, H. & GERSTEN, K. 2016 Boundary-Layer Theory. Springer.

- SEQUEIROS, O.E., SPINEWINE, B., BEAUBOUEF, R.T., SUN, T., GARCÍA, M.H. & PARKER, G. 2010 Characteristics of velocity and excess density profiles of saline underflows and turbidity currents flowing over a mobile bed. *J. Hydraul. Engng* **136** (7), 412–433.
- SIMPSON, J.E. 1999 *Gravity Currents: In the Environment and the Laboratory*. Cambridge University Press. SPALDING, D.B. 1954 Mass transfer in laminar flow. *Proc. R. Soc. Lond. A: Math. Phys. Sci.* **221** (1144), 78–99.
- THORPE, S.A. & LIU, Z. 2009 Marginal instability? J. Phys. Oceanogr. 39 (9), 2373-2381.
- TURNER, J.S. 1986 Turbulent entrainment: the development of the entrainment assumption, and its application to geophysical flows. *J. Fluid Mech.* **173**, 431–471.
- VERSTAPPEN, R.W.C.P. & VELDMAN, A.E.P. 2003 Symmetry-preserving discretization of turbulent flow. J. Comput. Phys. 187 (1), 343–368.
- WEI, T., WANG, Y. & YANG, X.I.A. 2021 Layered structure of turbulent plane wall jet. *Intl J. Heat Fluid Flow* 92, 108872.
- WELLS, M.G. 2007 Influence of Coriolis forces on turbidity currents and sediment deposition. In *Particle-Laden Flow: From Geophysical to Kolmogorov Scales* (ed. B.J. Geurts, H. Clercx & W. Uijttewaal), ERCOFTAC Series, pp. 331–343. Springer.
- WELLS, M., CENEDESE, C. & CAULFIELD, C.P. 2010 The relationship between flux coefficient and entrainment ratio in density currents. *J. Phys. Oceanogr.* 40 (12), 2713–2727.
- WYGNANSKI, I., KATZ, Y. & HOREV, E. 1992 On the applicability of various scaling laws to the turbulent wall jet. *J. Fluid Mech.* **234**, 669–690.
- YAO, J., CHEN, X. & HUSSAIN, F. 2022 Direct numerical simulation of turbulent open channel flows at moderately high Reynolds numbers. *J. Fluid Mech.* **953**, A19.